Journal of Engineering Science and Technology
Vol. 16, No. 2 (2021) 1386 - 1401

DESIGN AND EVALUATION OF A TRANSRECTAL PHASED PIEZOELECTRIC MICROMACHINED ULTRASOUND TRANSDUCER (PMUT) ARRAY FOR THERMAL TREATMENT OF PROSTATE CANCER

KHALDON LWEESY[1,*], MALAK FORA[1], HOSSAM EL-KHALIL[1], SRI-RAJASEKHAR KOTHAPALLI[2], AJAY DANGI[2]

[1]Department of Biomedical Engineering,
Jordan University of Science and Technology, Irbid 22110, Jordan
[2]Department of Biomedical Engineering,
The Pennsylvania State University, University Park, PA 16802, USA
*Corresponding Author: klweesy@just.edu.jo

Abstract

This paper describes a simulation study of designing a two-dimensional (2D) ultrasound phased piezoelectric micromachined ultrasound transducer (PMUT) arrays to be used for thermal treatment of prostate cancer. With 2D phased PMUT arrays, the location of the focal point can be precisely controlled by varying the elements' driving information (phase and power) which gives the ability to generate focal points and steer them electronically in a three-dimensional volume. Compared to piezoelectric (PZT) ultrasound transducers, PMUTs cost less, need less power to drive, smaller in size, and better in acoustic impedance matching. Different frequency/diameter pairs were considered in the study. For each frequency/diameter pair, different 2D arrays of size m x m was considered where each element in the array was considered a thin circular clamped plate. For each case, the maximum depth of penetration (DOP) and the maximum possible steering angle were reported. Optimal designs, that took into consideration PMUT parameters and prostate physical parameters, were sought. The study concluded that in order to achieve a PMUT array design that can generate focal points and fully steer them in the whole prostate (a steering angle of at least 21.25° and a maximum DOP of at least 4.5 cm), the optimal PMUT design must operate at a frequency less than 0.75 MHz and it must include at least 90 x 90 elements. Thus, the proposed technique allows for far distance ablation non-invasively and with higher steering angle ranges by using small size PMUT array.

Keywords: HIFU, Prostate cancer, PMUT, Ultrasound array.

1. Introduction

In the United States alone, the prevalence of prostate cancer in men was 0.11 % and the percentage of deaths was 0.019 % per year according to the National Cancer Institute 2012-2016 cases and deaths statistics (National Cancer Institute 2019) [1].

Various techniques used to treat prostate cancer including focus surgery, chemotherapy, radiotherapy, and surgery, with surgery being mostly used compared to other modalities because it is more efficient and has less side effects. There are also many complications in surgical techniques that occur in 25% of the treated cases, including urinary tract infections, incontinence, impotence, which often require long hospitalization [2, 3].

The use of high-intensity focused beams to treat prostate cancer has gained a lot of momentum in the past decade because it is non-invasive. Ultrasound or microwave beams are generated with such a technique to raise up the temperature of the targeted volume to 60°C for a short period of time (1 to 3 seconds). At high frequencies, the penetration depth of microwaves is very shallow. However, at low frequencies, the ability to generate a significant focus is jeopardized. This fact makes it less attractive [4, 5] to use microwave devices and more attention was given to ultrasound [6-10].

High intensity focused ultrasound (HIFU) converges the ultrasound wave all the way to its focal point, which could be achieved by different methods such as geometric focusing using a spherically curved source [11, 12], focusing using acoustic lens [13] or focusing the beam electronically by having multi elements that are driven by phase shifted sinusoids [14, 15]. With HIFU, short sonication (1 to 3 seconds) is applied at the targeted volume to noninvasively ablate the targeted tissues by raising their temperature to around 60°C [6-8]. The size of the generated focal region is usually much smaller than the cancerous volume to be ablated, making it crucial for the HIFU device to have the capability to focus and steer the ultrasound waves. With phased arrays, this problem is solved by altering the phase and power that drive the array's individual elements to focus and steer the ultrasound wave from one position to another. Previously designed prostate ultrasound devices used mechanical and electrical steering capabilities [14-18]. Such devices use piezoelectric (PZT) materials to generate ultrasound waves.

The use of PZT has many disadvantages including bulky devices, high power consumption, high noise levels, and the need to build matching and backing layers for the device [19]. Having these drawbacks in mind and with the advancement in technology in recent years, a lot of attention is given to micromachined ultrasound transducers (MUTs) built using microelectromechanical systems (MEMS) technology for advanced sensors and actuators. The most popular MUTs are the capacitive MUTs (CMUTs) and the piezoelectric MUTs (PMUTs) [19].

MUTs cost less, require less power consumption, miniaturized in size, and have better acoustic impedance matching to tissue. CMUTs are suitable only for high frequency applications ($>$1 MHz) and require high bias voltage to be excited ($\sim$ 100 V). PMUTs overcome these inherent drawbacks of CMUTs; they are suitable for low- to mid-range frequencies (40 kHz $<$ f $<$ 4 MHz) and do not require bias voltage [20, 21].

HIFU is used to treat different cancer types, prostate cancer is among theses. The prostate is a small gland which is part of the male's reproduction system. The

prostate has almost about the same size and shape of a walnut in normal young men (about 3.5 cm in diameter, 20-25 gm in mass). It is approximately 1 cm from the rectal wall, which makes it a non-invasive access to the prostate.

Problems with the previously designed arrays for HIFU include the need for complicated methods to change the focus or having limited focusing and steering capabilities. Such drawbacks were the impetus for designing a new array that can be used in thermal therapy of the prostate and can generate focal points and steer them in a systematic controlled manner with an acceptable grating lobes level. This paper illustrates the design of a PMUT two-dimensional phased array which is able to focus and steer ultrasonic beams in a three-dimensional (3D) volume for the purpose of treating prostate cancer.

2. Materials and Methods

2.1. Acoustic intensity simulations

MATLAB simulation was used to define the best size, shape, and number of the elements of the array, as well as to determine the device's pressure and temperature fields. After running MATLAB simulations for different element sizes and different element numbers and taking into consideration the physical constraints of the prostate size and location, the intersection of the resultant curves determines the optimized array size and its number of elements that must be used. The output acoustic pressure from m x m two dimensional (2D) square axisymmetric PMUT array is considered. Only elements that fit in a circular shape are considered active while the remaining elements are considered inactive as shown in Fig. 1(a). All individual elements are assumed to be thin circular clamped plates; having the same diameter and are spaced by 50 μm. Figure 1(b) shows a side view of each of the circular elements of the array.

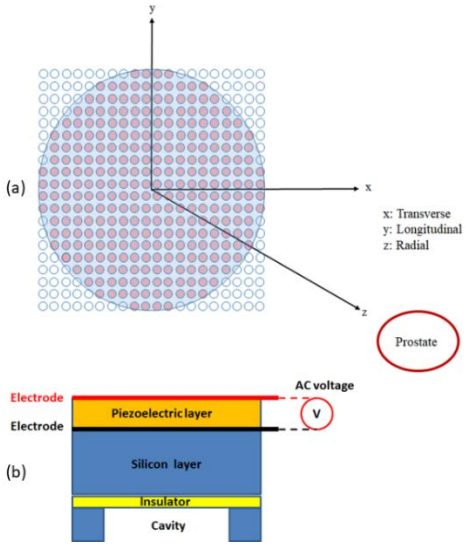

Fig. 1. (a) Front view diagram of the simulated 2D PMUT array; and (b) side view of each of the circular elements of the array.

Each element of the PMUT array is considered as a circular piston that is composed of a thin PZT layer sandwiched between two electrodes, and a thicker silicon layer. To drive each element, a sinusoidal input voltage is applied across the PZT layer using two electrodes; this will cause the plate to vibrate producing a mechanical pressure. A silicon layer was used for resonance frequency calculation where the effect of thinner layers can be neglected. For a single material plate, the first mode (0, 1) resonance frequency f is calculated using the formula in [22]:

$$f = 0.4671 \frac{h}{a^2} \sqrt{\frac{Y}{\rho(1-\upsilon^2)}} \quad (1)$$

where h is the layer thickness, a is the plate radius, Y is the Young's modulus, ρ is the plate material density and υ is the Poisson's ratio. The values of these constants for silicon are listed in Table 1 [23].

Table 1. The values of the constants of Eq. (1) for silicon.

Parameter	h(µm)	Y (GPa)	ρ (kg/m^3)	υ
Value	5	169	2329	0.064

Equation (1) was used to plot the frequency/ diameter pairs to be studied. Figure 2 shows a plot of the resonance frequency of the piston in MHz versus its diameter in µm.

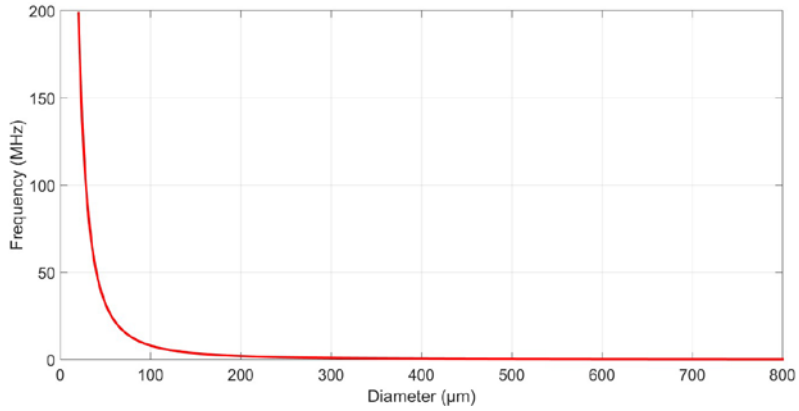

Fig. 2. Frequency versus diameter plot for a PMUT circular piston.

Different frequency/diameter pairs were used to study the maximum depth of penetration (DOP), basically by introducing the attenuation as a function of frequency, and maximum steering angle for each simulated array. Table 2 shows the frequency/diameter pairs considered in this study.To help in evaluating the far field pressure distribution generated from a single element circular piston, additional coordinates are introduced as shown in Fig. 3.

To help in evaluating the far field pressure distribution generated from a single element circular piston, additional coordinates are introduced as shown in Fig. 3.

Table 2. Frequency/ diameter pairs considered

Diameter (μm)	Frequency (MHz)
80	12.41
100	7.942
150	3.53
200	1.985
250	1.271
300	0.8824
350	0.6483
400	0.4963
450	0.3922
500	0.3177
550	0.2625
600	0.2206
650	0.188
700	0.1621
750	0.1412
800	0.1241

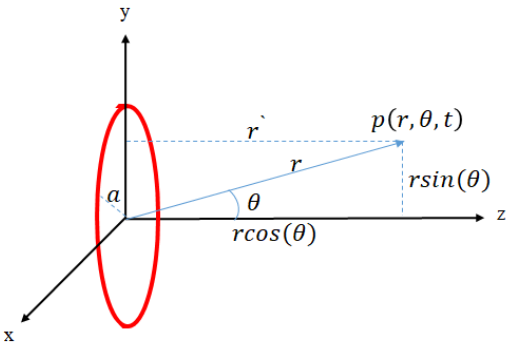

Fig. 3. PMUT single element piston coordinates, adopted from [24].

The far field pressure distribution consists of three parts: the pressure magnitude part, the angular dependent part, and the phase and oscillation part, and is given by [24]:

$$p(r,\theta,t) = \underbrace{\frac{j}{2}\rho_o c U_o \frac{a}{r} ka}_{\text{pressure magnitude part}} . \underbrace{\left[\frac{2J_1(kasin\theta)}{kasin\theta}\right]}_{\text{angular dependent part}} . \underbrace{e^{j(\omega t - kr + \emptyset)}}_{\text{phase and oscillation part}} \quad (2)$$

where ρ_o is equilibrium density of the medium at the point (r, θ) in kg/m^3, c is the sound's speed in the medium in m/s, U_o is the peak normal speed of the piston in m/s, a is the radius of the piston in m, k is the wave number in m^{-1}, ω is the radian frequency in rad/s, and $\emptyset$ is the element phase in rad. For the sake of clarification, an example of a circular piston with a ka value of 10 is considered. The pressure

magnitude part and the angular dependent part for this case were plotted in Fig. 4(a) and Fig. 4(b), respectively.

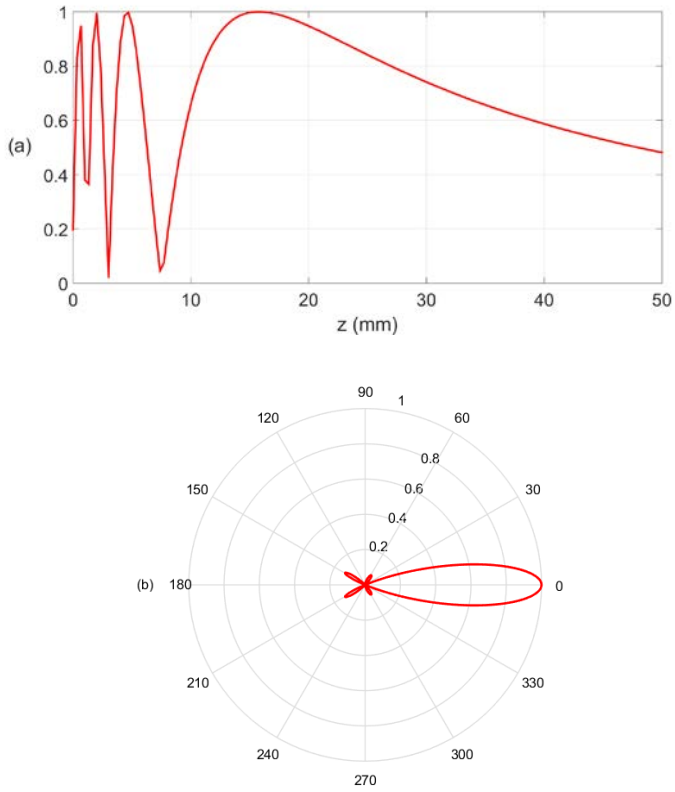

Fig. 4. (a) The pressure magnitude part; and (b) the angular dependent part for a circular piston with a *ka* value of 10.

For any circular piston element, the f-number ($f_{\#}$) represents an important design parameter. It is defined as the ratio of the distance of the piston's last peak value to the piston's diameter($f_{\#} = r_1/d$).

2.1.1. Focusing and steering of ultrasound waves

Each element (i) of the array was driven by a certain phase value ($\emptyset i$). The phase values were calculated so that the sinusoidal pressure waves from all the elements arrive at the intended focal point in phase, which will make the pressure at the focal point to be maximum. The phase values were calculated using:

$$\emptyset_i = \frac{360^o}{\lambda}(d_i - d_o) - 360^o n \quad (3)$$

where λ is the wavelength in m, d_o is the distance from the focal point to the center of the transducer in m, d_i is the distance from the focal point to the center of element i in m, and n is an integer that is used to ensure that the phase lies between 0° and 360°.

Driving each element (i) with the corresponding phase value ($\emptyset i$) introduces a time delay to each element that corresponds to the difference in distance between d_i and d_o. As a result, the ultrasound beams generated by the individual elements of the array will arrive at the targeted focal point location in phase. Except for the targeted focal point location, where all the contributions of the individual elements of the array are maximum due to the in-phase arrival of their beams at the focal point, all other locations in tissue will observe out of phase contributions, which will result in having a maximum pressure value only at the intended location [25].

The ability of the array to focus and steer in three dimensions is to be checked. Since the array is axisymmetric, pressure calculation in the *xz*-plane is sufficient to do that. Analysis was done on the *xz*-plane where Huygen's principle was implemented to calculate the total pressure distribution by summing up the contributions of many simple sources [26]. As a result, the total pressure $p(x, y, z)$ at any point in the volume of interest can be calculated by discretizing the Rayleigh–Sommerfeld equation:

$$p(x,y,z) = \sum_{i=1}^{n^2} \sqrt{\frac{2P\rho}{cA}} \left(\frac{fS}{d_i}\right) \exp\left[j\left(\emptyset_i - \frac{2\pi d_i}{\lambda}\right) - d_i\alpha\right] \quad (4)$$

where ρ is the medium density in Kg/m^3, c is sound speed in m/s, A is the PMUT array overall surface area in m^2, P is the overall acoustic power generated by the array (W), f is the operating frequency (Hz), S is the i^{th} element's area (m^2), α is the attenuation coefficient (Np/m/MHz), and d_i and $\emptyset i$ are as in Eq. (3).

When trying to focus the ultrasound beam off the main axis (off-axis focusing), grating lobes artifacts will be generated. Since the steering angle increases with increasing the location of the off-axis focus, the Grating lobes peak value increases nonlinearly with increasing the steering angle. In therapeutic ultrasound, the maximum observed Grating lobe value should not exceed –8.24 dB of the focal point's peak intensity. An example of the simulations performed in this regard is shown in Fig. 5, where for the second case considered (Table 2) the focus was aimed at (0, 0, 10) mm, (2, 0, 10) mm, (4, 0, 10) mm, (6, 0, 10) mm, (8, 0, 10) mm, and (10, 0, 10) mm, as shown in Figs. 5(a)-5(f) respectively. The corresponding steering angles were 0°, 11.3°, 21.8°, 31.0°, 38.7°, and 45°, respectively, and the corresponding observed simulated Grating lobe values were –40.0 dB, –13.0 dB, –9.0 dB, –5.6 dB, –2.4 dB, and –2.0 dB, respectively. The first three Grating lobe values are acceptable since they are less than the –8.24 dB threshold while the other three values are not. Grating lobe values that exceed the –8.24 dB threshold result in increasing the temperature to harmful limits at unintended locations thus one needs to make sure not to exceed that –8.24 dB threshold value.

For each of the considered square array size dimensions (100x100, 90x90, 80x80, 70x70, 60x60, 50x50, and 40x40), the frequency and diameter of the array elements were varied according to the frequency/ diameter pairs shown in Table 2. The steering angle was controlled by the phase information entered to the phased array. Starting from 0° phase (on-axis focusing), the phase information was changed to increase the steering angle by increments of 1° until a Grating lobe value of –8.24 dB or more is observed, and that was considered as the maximum steering angles as shown in Fig. 6.

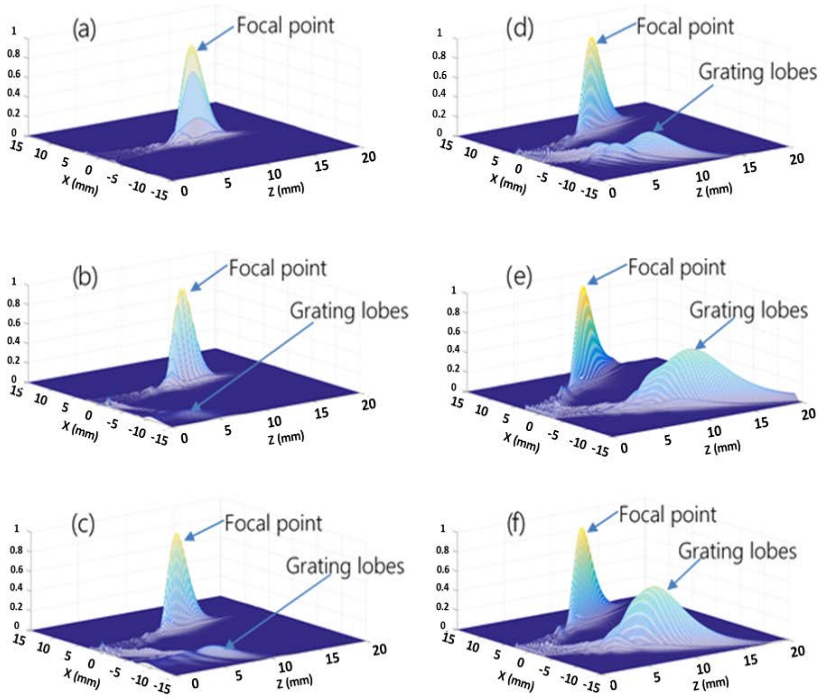

Fig. 5. (a) On-axis focusing at (0, 0, 10) mm and Off-axis focusing at; (b) (2, 0, 10) mm; (c) (4, 0, 10) mm; (d) (6, 0, 10) mm; (e) (8, 0, 10) mm; and (f) (10, 0, 10) mm, showing for each case the intended focal point and the unintended Grating lobe.

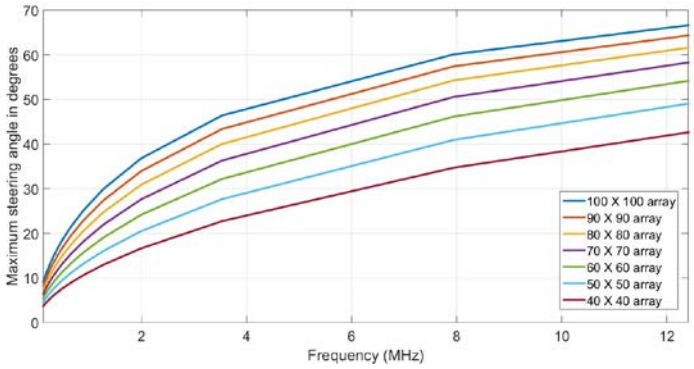

Fig. 6. The maximum steering angle as a function of frequency for the array sizes of 100x100, 90x90, 80x80, 70x70, 60x60, 50x50, and 40x40.

2.1.2. Depth of penetration (DOP) for the array

For each of the sixteen frequency-diameter pairs considered in this study (Table 2), square array sizes of dimensions of 100x100, 90x90, 80x80, 70x70, 60x60, 50x50, and 40x40 were simulated to determine the maximum DOP, which can be calculated as follows:

$$I(r) = I_o e^{-2\alpha r} \quad (5)$$

where *I(r)* is the intensity at point *r* along the z-axis (W/m^2), I_o is the initial intensity (W/m^2), *r* is the travelled distance (m) along the *z*-axis, and α is the attenuation coefficient in dB/MHz/m. α was considered to be 70 dB/MHz/m, which is the value of the attenuation coefficient in soft tissue.

The attenuation coefficient (α) has a unit of dB/MHz/m which clearly indicates that the attenuation of ultrasound waves depends on both frequency and travelled distance. A plot of the normalized intensity vs. travelled distance for the sixteen different frequencies considered (Table 2) is shown in Fig. 7(a). Assuming a dynamic range of the array to be 40 dB, the simulated results plotted in Fig. 7(a) were used to find the maximum DOP for each of the sixteen frequencies considered. A plot of the maximum DOP vs. frequency is shown in Fig. 7(b).

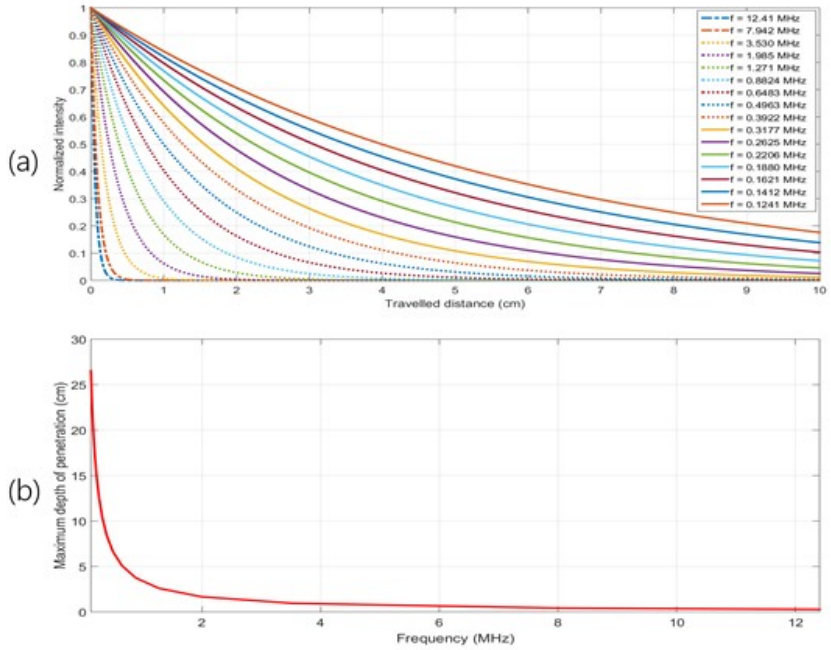

Fig. 7. (a) The normalized intensity vs. travelled distance for the sixteen different frequencies considered: and (b) the resultant maximum DOP vs. frequency.

2.2. Temperature simulations

From the obtained pressure field and intensity simulations, the temperature distribution was simulated using the Pennes' bioheat transfer equation (BHTE) [27, 28]:

$$\rho C_t \frac{\partial T}{\partial t} = K\left(\frac{\partial^2 T}{\partial x^2} + \frac{\partial^2 T}{\partial y^2} + \frac{\partial^2 T}{\partial z^2}\right) - wC_b(T - T_a) + Q(x, y, z) \quad (6)$$

where ρ is the density of the medium (Kg/m^3), C_t is the specific heat of the tissue which equals 3770 J/kg/°C, *T* is the temperature in °C at the point *x*, *y*, *z* at time *t*, *K* is the thermal conductivity which equals 0.5 W/m/°C, T_a is the arterial blood temperature which equals 37°C, *w* is the tissue perfusion in kg/m^3/s, C_b is the blood specific heat

which equals 3770 J/kg/°C and $Q(x, y, z)$ is the deposited power at the location (x, y, z) which was estimated using the array's resultant simulated intensity using:

$$I(x,y,z) = \frac{1}{T}\int_0^T I(t,x,y,z)dt = \frac{1}{T}\int_0^T \frac{1}{\rho c}p^2(t,x,y,z)dt = \frac{P^2(x,y,z)}{2\rho c} \quad (7)$$

$$Q(x,y,z) = \alpha I(x,y,z) = \alpha\frac{P^2(x,y,z)}{2\rho c} \quad (8)$$

To reduce the simulation time, the BHTE (Eq. (6)) was solved numerically on planes of interest (*xz*-planes). The boundary conditions were set by assuming that there is no heat transfer between the thermodynamic system and the surroundings (adiabatic boundary conditions); that is to say $\partial T/\partial x = \partial T/\partial z = 0$.

The initial condition for the temperature (T) was set to 37°C over the whole boundary ($T(x,z) = 37$°C). To numerically solve the BHTE, explicit finite difference method was used:

$$\rho C_t\frac{T_{i,j}^{n+1}-T_{i,j}^n}{\Delta t} = K\left[\frac{T_{i+1,j}^n-2T_{i,j}^n+T_{i-1,j}^n}{\Delta x^2}+\frac{T_{i,j+1}^n-2T_{i,j}^n+T_{i,j-1}^n}{\Delta z^2}\right] - wC_b\left[T_{i,j}^n - T_a\right] + \dot{Q}_{i,j} \quad (9)$$

For three of the six cases described in Fig. 5, the BHTE was solved numerically, and the temperature distributions were simulated. The heat source was kept ON for 3 seconds since HIFU treatments use short sonication (from 1 to 3 seconds). For a focal point aimed at (0, 0, 10) mm (Fig. 5(a)) the simulated temperature profile showed that temperature reached a value of 53°C at the center of the focal point, while remaining within the safety limits at all other locations. Figures 8(a) and 8(b) show the simulated temperature profile as a mesh plot and a contour plot, respectively, while Figs. 8(c) and 8(d) show the temperature plots at the two cross sections shown in Fig. 8(b). For a focal point aimed at (2, 0, 10) mm (Fig. 5(b)), similar plots are shown in Figs. 9(a)-9(d) which show that except at the intended focal point, the temperature values remain around 37°C. A third temperature simulation is performed for the case of a focal point aimed at (6, 0, 10) mm (Fig. 5(d)) and the resultant plots are shown in Figs. 10(a)-10(d). The presence of the Grating lobes in the original intensity profile resulted in unsafe temperature values and as a result this point was considered outside the maximum steering angle for this array.

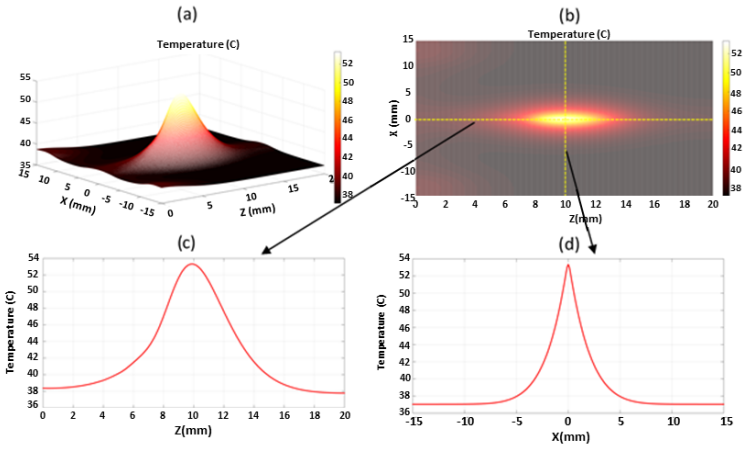

Fig. 8. Temperature plots for the case of a focal point aimed at (0, 0, 10) mm as (a) mesh; (b) contour; (c) cross section over the *z*-axis; and (d) cross section over the *x*-axis.

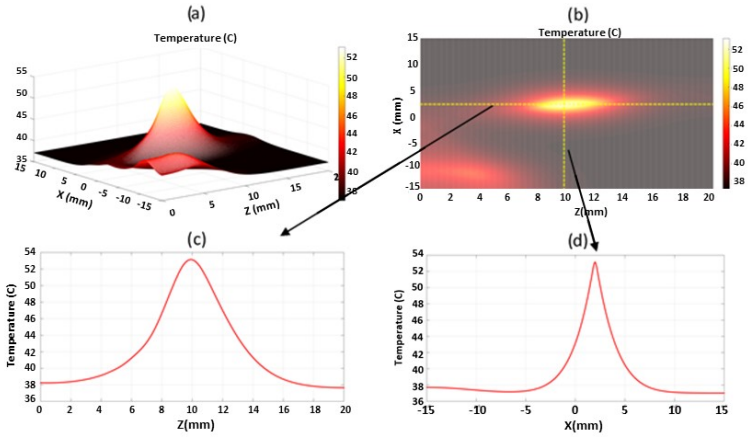

Fig. 9. Temperature plots for the case of a focal point aimed at (2, 0, 10) mm as (a) mesh; (b) contour; (c) cross section over the *z*-axis; and (d) cross section over the *x*-axis.

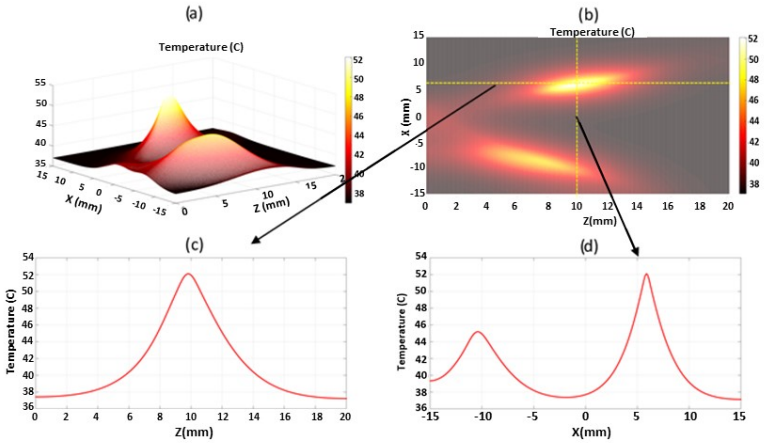

Fig. 10. Temperature plots for the case of a focal point aimed at (6, 0, 10) mm as (a) mesh; (b) contour; (c) cross section over the *z*-axis; and (d) cross section over the *x*-axis.

3. Results

Figure 6 is a plot of the maximum steering angle as a function of frequency for the array sizes of 100x100, 90x90, 80x80, 70x70, 60x60, 50x50, and 40x40. It shows that for any array size, the maximum steering angle increases with frequency. It also shows that at a specific frequency, the maximum steering angle increases with increasing the array's number of elements. It clearly indicates that increasing the number of elements of the array increases the maximum steering angle of the array. For example, at a frequency of 2 MHz, a 40x40 array has a maximum steering angle of 17° while a 100x100 array has a maximum steering angle of 37°. Figure 7(a) shows that the ultrasound intensity attenuates exponentially when distance increases (at a fixed frequency) and it also attenuates exponentially when frequency decreases (at a fixed distance); while Fig. 7(b) shows that the maximum DOP is inversely proportional to frequency. For example, at

a frequency of 2 MHz, the maximum DOP is about 1.75 cm while at a frequency of 1 MHz, the maximum DOP is about 3.70 cm.

Since the choices of frequency and number of elements affect directly the maximum steering angle and the maximum DOP, physical constraints of the prostate have to be studied to find the optimal design that can be used for prostate cancer HIFU treatment. The prostate is approximately the same size as a walnut (about 3.5 cm in diameter) and about 1 cm away from the rectal wall. As a result, the optimal design must have a maximum DOP of at least 4.5 cm. Considering that the prostate is about 3.5 cm in diameter and that the maximum DOP is at least 4.5 cm, the optimal design must have a steering angle of at least tan-1(3.5/2/4.5) = 21.25º.

Figure 6 is replotted again in Fig. 11(a) with the optimal design region highlighted taking into consideration the maximum steering angle of at least 21.25°. Figure 7(b) was also replotted again in Fig. 11(b) with the optimal DOP region highlighted. The intersection of the two highlighted regions is plotted in Fig. 11(c). Table 3 lists the associated DOP's with their corresponding frequencies.

The combined results of Fig. 11(c) and Table 3 indicate that in order to completely being able to focus and steer in the whole volume of the prostate, the frequency must be ≤ 0.75 MHz (linear interpolation was used on the two bolded values in Table 3) and the number of array elements should be at least 90 x 90.

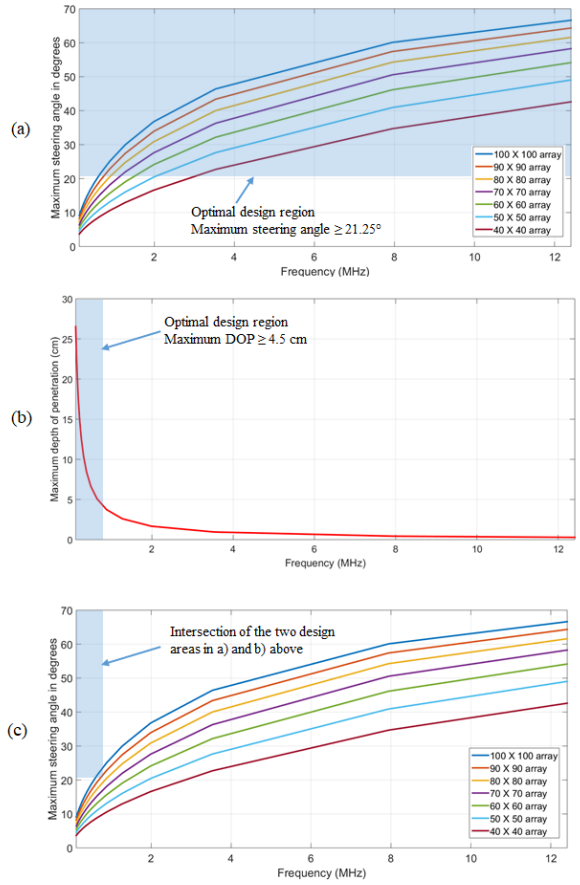

Fig. 11. (a) The optimal design region considering a maximum steering angle of 21.25° or more; (b) the optimal design region considering a maximum DOP of 4.5 cm or more; and (c) the intersection of the two curves in (a) and (b).

Table 3. Frequencies considered and their associated DOP.

Frequency (MHz)	DOP (cm)	Frequency (MHz)	DOP (cm)
12.41	0.28	0.3922	8.4
7.942	0.43	0.3177	10.37
3.53	0.95	0.2625	12.55
1.985	1.67	0.2206	14.93
1.271	2.6	0.188	17.51
0.8824	3.74	0.1621	20.31
0.6483	5.09	0.1412	23.31
0.4963	6.64	0.1241	26.52

4. Conclusions

Intra-cavitary ultrasound devices have shown promising results in treating prostate cancer thermally by electronically focusing the ultrasound beam and steering it electronically at the targeted volume. Compared to other modalities, the use of intra-cavitary ultrasound has many advantages; it is non-invasive, has fewer complications, and has short treatment time. One compelling explanation for using intra-cavitary ultrasonic devices is the close proximity of the prostate gland to the rectal wall via the rectum, which allows heating the targeted volume in the prostate noninvasively without causing damage to healthy tissues. The use of PMUT phased arrays to move the location of the focal point (focus or steer) by means of electrical phase and power control gives the ability to control the deposition of the power in tissue and significantly minimize the time required to perform the whole treatment since the focal point is moved in an electronic way rather than the manual way.

PMUT diameter frequency relationships as well as physical shape and location of the prostate have been considered in this simulation study, which concluded that, for a prostate that is 3.5 cm in diameter and 1 cm away from the rectal wall, the optimal PMUT design must operate at a frequency less than 0.75 MHz and it must include at least 90x90 elements. Not meeting theses specifications means that at least one of the two crucial design values (the maximum DOP and the maximum steering angle) will not be satisfied. In case the prostate was more than 3.5 cm in diameter or was more than 1 cm away from the rectal wall, more number elements will be needed to achieve a higher steering angle and a lower frequency is needed to achieve a higher DOP.

Acknowledgment

This work was supported by the Deanship of Research at Jordan University of Science and Technology and the Department of Biomedical Engineering at the Pennsylvania State University.

Nomenclatures

A	The PMUT array overall surface area, m^2

a	Plate radius, μm
C_b	Blood specific heat, J/kg/^{o}C
C_t	Specific heat of the tissue, J/kg/^{o}C
c	Speed of sound in the medium, m/s
d_i	Distance from the focal point to the centre of element, m
d_o	Distance from the focal point to the centre of the transducer, m
f	Resonance frequency, MHz
$f_\#$	F-number
h	Layer thickness, μm
I	Intensity, W/m^2
K	thermal conductivity, W/m/^{o}C
k	Wave number, m^{-1}
P	Acoustic power, W
p	Acoustic pressure
Q	Deposited power, W
r	Distance along z-axis, m
S	Element area, m^2
T	Temperature, ^{o}C
T_a	Arterial blood temperature, ^{o}C
U_o	Peak normal speed of the piston, m/s
w	Tissue perfusion, kg/m^3/s
Y	Young's modulus, GPa

Greek Symbols

α	Attenuation coefficient, Np/m/MHz
θ	Steering angle, deg.
λ	Wavelength, m
ρ_o	Equilibrium density of the medium, Kg/m^3
ρ	Material/ medium density, kg/m^3
υ	Poisson's ratio
$\emptyset$	Element phase value, rad
ω	Radian frequency, rad/s

Abbreviations

2D	Two dimensional
3D	Three dimensional
BHTE	Pennes' bioheat transfer equation
CMUT	Capacitive Micromachined Ultrasonic Transducer
DOP	Depth of Penetration
HIFU	High Intensity Focused Ultrasound
MEMS	Microelectromechanical systems
MUT	Micromachined Ultrasonic Transducer
PMUT	Piezoelectric Micromachined Ultrasonic Transducer
PZT	Piezoelectric

References

1. National Cancer Institute at the National Institutes of Health, Cancer Statistics (2019).

2. Michaelson, M.D.; Cotter, S.E.; Gargollo, P.C., Zietman, A.L.; Dahl, D.M.; and Smith, M.R. (2008). Management of complications of prostate cancer treatment. *A Cancer Journal for Clinicians*, 58(4), 196-213.
3. Tewari, A.; Sooriakumaran, P.; Bloch, D.A.; and Seshadri-Kreaden, U. (2012). Positive surgical margin and perioperative complication rates of primary surgical treatments for prostate cancer: A systematic review and meta-analysis comparing retropubic, laparoscopic, and robotic prostatectomy. *European Urology*, 62(1), 1-15.
4. Shinohara, K. (2004) Thermal ablation of prostate diseases: Advantages and limitations. *International Journal of Hyperthermia*, 20(7), 679-697.
5. Saleh, K.Y. (2004). *Design and evaluation of multi-dimensional ultrasound phased arrays for thermal treatment of prostate diseases*. Ph.D. Thesis. The Pennsylvania State University, Pennsylvania.
6. Mistry, K.; Reddy, U.; Bott, S.; Emara, A.; and Hindley, R. (2017). MP70-11 Medium term outcomes following focal hifu for the treatment of localised prostate cancer: A single centre experience. *The Journal of Urology*, 197(4S), e939.
7. Hardenberg, J.V.; Westhoff, N.; Baumunk, D.; Hausmann, D.; Martini, T.; Marx, A.; Porubsky, S.; Schostak, M.; Michel, M.S.; and Ritter, M. (2018). Prostate cancer treatment by the latest focal HIFU device with MRI/TRUS-fusion control biopsies: A prospective evaluation. *In Urologic Oncology: Seminars and Original Investigations*, 36(9), 401.e1-401.e9.
8. Crouzet, S.; Blana, A.; Murat, F.J.; Pasticier, G.; Brown, S.C.; Conti, G.N.; Ganzer, R.; Chapet, O.; Gelet, A.; Chaussy, C.G.; Robertson, C.N.; Thuroff, S.; and Ward, J.F. (2017). Salvage high-intensity focused ultrasound (HIFU) for locally recurrent prostate cancer after failed radiation therapy: Multi-institutional analysis of 418 patients. *BJU International*, 119(6), 896-904.
9. Beckler, B.; Cowan, A.; Farrar, N.; Murawski, A.; Robinson, A.; Diamanduros, A.; Scarpinato, K.; Sittaramane, V.; and Quirino, R.L. (2018). Microwave heating of antibody-functionalized carbon nanotubes as a feasible cancer treatment. *Biomedical Physics and Engineering Express*, 4(4), 045025.
10. Park, J.Y.; Choi, P.; Kim, H.K.; Kang, K.S.; and Ham, J. (2016). Increase in apoptotic effect of Panax ginseng by microwave processing in human prostate cancer cells: in vitro and in vivo studies. *Journal of Ginseng Research*, 40(1), 62-67.
11. Bini, F.; Trimboli, P.; Marinozzi, F.; and Giovanella, L. (2018). Treatment of benign thyroid nodules by high intensity focused ultrasound (HIFU) at different acoustic powers: a study on in-silico phantom. *Endocrine*, 59(3), 506-509.
12. Rosnitskiy, P.B.; Yuldashev, P.V.; Sapozhnikov, O.A.; Maxwell, A.D.; Kreider, W.; Bailey, M.R.; and Khokhlova, V.A. (2016). Design of HIFU transducers for generating specified nonlinear ultrasound fields. *IEEE Transactions on Ultrasonics, Ferroelectrics, and Frequency Control*, 64(2), 374-390.
13. Xia, J.P.; Zhang, X.T.; Sun, H.X.; Yuan, S.Q.; Qian, J.; and Ge, Y. (2018). Broadband tunable acoustic asymmetric focusing lens from dual-layer metasurfaces. *Physical Review Applied*, 10(1), 014016.
14. Zhang, H.; Zhang, Y.; and Jian, X. (2019). Phased Transducer and Drive System Design. *2019 IEEE International Conference on Computational*

Intelligence and Virtual Environments for Measurement Systems and Applications (CIVEMSA).1-4.

15. Kuo, L.W.; Chiu, L.C.; Lin, W.L.; Chen, J.J.; Dong, G.C.; Chen, S.F.; and Chen, G.S. (2018). Development of an MRI-compatible high-intensity focused ultrasound phased array transducer dedicated for breast tumor treatment. *IEEE Transactions on Ultrasonics, Ferroelectrics, and Frequency Control*, 65(8), 1423-1432.
16. Chaussy, C.G.; and Thüroff, S. (2017). High-intensity focused ultrasound for the treatment of prostate cancer: A review. *Journal of Endourology*, 31(1), S-30-S-37.
17. Chopra, R.; Colquhoun, A.; Burtnyk, M.; N'djin, W.A.; Kobelevskiy, I.; Boyes, A.; Siddiqui, K.; Foster, H.; Sugar, L.; Haider, M.A.; and Bronskill, M. (2012). MR imaging–controlled transurethral ultrasound therapy for conformal treatment of prostate tissue: initial feasibility in humans. *Radiology*, 265(1), 303-313.
18. Curiel, L.; Chavrier, F.; Souchon, R.; Birer, A.; and Chapelon, J.Y. (2002). 1.5-D high intensity focused ultrasound array for non-invasive prostate cancer surgery. *IEEE Transactions on Ultrasonics, Ferroelectrics, and Frequency Control*, 49(2), 231-242.
19. Jung, J.; Lee, W.; Kang, W.; Shin, E.; Ryu, J.; and Choi, H. (2017). Review of piezoelectric micromachined ultrasonic transducers and their applications. *Journal of Micromechanics and Microengineering*, 27(11), 113001.
20. Wang, T.; Kobayashi, T.; Yang, B.; Wang, H.; and Lee, C. (2016). Highly sensitive piezoelectric micromachined ultrasonic transducer (pMUT) operated in air. *IEEE 11th Annual International Conference on Nano/Micro Engineered and Molecular Systems (NEMS)*. Matsushima Bay and Sendai MEMS City, Japan, 294-299.
21. Percin, G.; and Khuri-Yakub, B.T. (2002). Piezoelectrically actuated flextensional micromachined ultrasound droplet ejectors. *IEEE transactions on ultrasonics, ferroelectrics, and frequency control*, 49(6), 756-766.
22. Smyth, K.M. (2012). *Design and modeling of a PZT thin film based piezoelectric micromachined ultrasonic transducer (PMUT)*. Doctoral dissertation, Massachusetts Institute of Technology, USA.
23. Suijlen, M.A.G.; and Woltjer, R. (2017). Time-dependent study of pressure waves generated by square array MEMS ultrasound transducers. *Proceedings of the COMSOL Conference in Rotterdam*. Rotterdam, Netherlands, 1-6.
24. Kinsler, L.E.; Frey, A.R.; Coppens, A.B.; and Sanders, J.V. (1999). *Fundamentals of acoustics* (4th ed.). John Wiley and Sons.
25. Shung, K.K. (2006). *Diagnostic ultrasound, imaging, and blood flow measurements* (2nd ed.). Taylor and Francis.
26. Zemanek, J. (1971). Beam behavior within the nearfield of a vibrating piston. *The Journal of the Acoustical Society of America*, 49(1B), 181-191.
27. Pennes, H.H. (1948). Analysis of tissue and arterial blood temperatures in the resting human forearm. *Journal of Applied Physiology*, 1(2), 93-122.
28. Smith, N.B.; Buchanan, M.T.; and Hynynen, K. (1999). Transrectal ultrasound applicator for prostate heating monitored using MRI thermometry. *International Journal of Radiation Oncology, Biology, and Physics*, 43(1), 217-225.